Since January 2020 Elsevier has created a COVID-19 resource centre with free information in English and Mandarin on the novel coronavirus COVID-19. The COVID-19 resource centre is hosted on Elsevier Connect, the company's public news and information website.

Sensors & Actuators: B. Chemical 365 (2022) 131974

Contents lists available at ScienceDirect

Sensors and Actuators: B. Chemical

journal homepage: www.elsevier.com/locate/snb

High-sensitivity and point-of-care detection of SARS-CoV-2 from nasal and throat swabs by magnetic SERS biosensor

Yanyan Li [a,b,c], Chenglong Lin [a,b,c], Yusi Peng [a,b,c], Jun He [d,e], Yong Yang [a,c,*]

[a] State Key Laboratory of High-Performance Ceramics and Superfine Microstructures, Shanghai Institute of Ceramics, Chinese Academy of Sciences, 1295 Dingxi Road, Shanghai 200050, People's Republic of China
[b] Graduate School of the Chinese Academy of Sciences, No.19(A) Yuquan Road, Beijing 100049, People's Republic of China
[c] Center of Materials Science and Optoelectronics Engineering, University of Chinese Academy of Sciences, Beijing 100049, China
[d] Anhui Provincial Center for Disease Control and Prevention, Hefei 12560, Anhui, People's Republic of China
[e] Public Health Research Institute of Anhui Province, Hefei 12560, Anhui, People's Republic of China

ARTICLE INFO

Keywords:
SERS biosensors
SARS-CoV-2
Magnetic enrichment and separation
Point-of-care detection
Support vector machine

ABSTRACT

The outbreak of COVID-19 caused by SARS-CoV-2 urges the development of rapidly and accurately diagnostic methods. Here, one high-sensitivity and point-of-care detection method based on magnetic SERS biosensor composed of Fe_3O_4-Au nanocomposite and Au nanoneedles array was developed to detect SARS-CoV-2 directly. Among, the magnetic Fe_3O_4-Au nanocomposite is applied to capture and separate virus from nasal and throat swabs and enhance the Raman signals of SARS-CoV-2. The magnetic SERS biosensor possessed high sensitivity by optimizing the Fe_3O_4-Au nanocomposite. More significantly, the on-site detection of inactivated SARS-CoV-2 virus was achieved based on the magnetic SERS biosensor with ultra-low limit of detection of 100 copies/mL during 15 mins. Furthermore, the contaminated nasal and throat swabs samples were identified by support vector machine, and the diagnostic accuracy of 100% was obtained. The magnetic SERS biosensor combined with support vector machine provides giant potential as the point-of-care detection tool for SARS-CoV-2.

1. Introduction

The outbreak of coronavirus disease 19 (COVID-19) induced by severe acute respiratory syndrome coronavirus 2 (SARS-CoV-2) has caused worldwide emergency because of its high infection [1,2]. With the implementation of the nucleic acid-based and serological diagnostic tests, such as reverse transcriptase polymerase chain reaction (RT-PCR) and enzyme-linked immunosorbent assay (ELISA), COVID-19 was suppressed by screening and diagnosing the suspected person and then isolating the virus carries [3–6]. However, both the nucleic diagnostic tests and the serological diagnostic tests face some challenges. For example, the present RT-PCR methods are time-consuming and usually costly due to the sophisticated equipment, well-trained personnel, and costly reagents [7–9]. Furthermore, it is worth noting that SARS-CoV-2 will produce the variant virus strains with high transmissibility, which will decrease the accuracy and specificity of the current detection technique [10]. In order to timely detect and control the spreading of SARS-CoV-2, reliable diagnostic methods need to be developed urgently. Surface Enhanced Raman Scattering (SERS) is a trace detection tool with high sensitivity, fast and simple detection process, which is already applied as biosensors to detect some biomolecules including cancer, virus, and bacteria currently [11–15]. The SERS biosensors possess a simpler and faster detection process compared to the most frequently used RT-PCR. So, the SERS biosensors are of great potential to control the severe epidemic.

However, the biological detection based on SERS faces a huge challenge, that is, the complicated biological environment will interfere and submerge the Raman signals of targets. For solving this problem, a bifunctional composite that combined magnetic beads and SERS-active materials was developed. The magnetic SERS sensors not only could specifically select and detect the targets in a complicated environment by modifying specific protein, but also could enrich objects and further increase the sensibility of SERS. Therefore, the magnetic SERS biosensors have been applied to the detection of biomacromolecules without interferences of physiological environment [16]. Yang Sun et al. developed a sandwich-structure consisting of SERS tags, target influenza

* Corresponding author at: State Key Laboratory of High-Performance Ceramics and Superfine Microstructures, Shanghai Institute of Ceramics, Chinese Academy of Sciences, 1295 Dingxi Road, Shanghai 200050, People's Republic of China.
E-mail address: yangyong@mail.sic.ac.cn (Y. Yang).

https://doi.org/10.1016/j.snb.2022.131974
Received 9 December 2021; Received in revised form 13 April 2022; Accepted 26 April 2022
Available online 28 April 2022

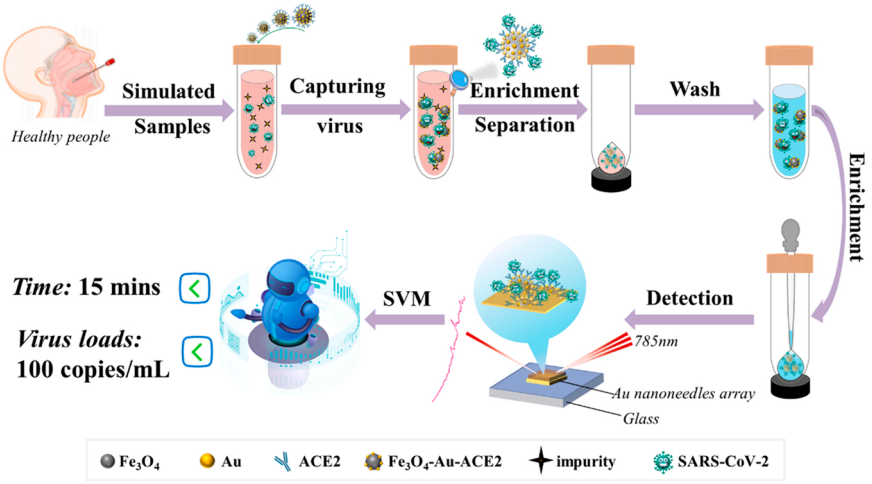

Scheme 1. The schematic diagram of SARS-CoV-2 virus detection process.

viruses and highly SERS-active magnetic supporting substrates for the detection of intact and inactivated influenza virus [17]. Tianxi Yang et al. prepared Fe_3O_4 @Au@Ag nanocomposite to detect Adenosine with the limit of detection (LOD) of 10^{-10} M. And the SERS protocol achieved the trace detection of Adenosine in urine with an azo coupling which could remove urea in urine [18]. Chongwen Wang et al. developed Fe_3O_4 @Ag SERS system combined with lateral flow immunoassay (LFIA) to detect influenza A H1N1 virus and human adenovirus (HAdV) simultaneously [19]. The SERS-based LFIA was 2000 times more sensitive than standard colloidal gold strip methods with 50 and 10 pfu/mL LOD for H1N1 and HAdV, respectively. Therefore, Fe_3O_4 @noble metal nanocomposite has a wide application in the biomolecule detection. However, the Fe_3O_4 @noble metal nanocomposite faces the challenge of low sensitivity. In order to increase the SERS enhancement, some mature SERS substrate is applied to combined with Fe_3O_4 @noble metal nanocomposite [17]. Besides, specific recognition and capturing of target molecules plays a vital role in the SERS detection. For the detection of SARS-CoV-2, Angiotensin-converting enzyme 2 (ACE2) was selected because of the nanomolar affinity between ACE2 and SARS-CoV-2 spike protein [20]. And, given the electrostatic interaction between His-ACE2 (short for ACE2 labelled Histidine) and Fe_3O_4, ACE2 could be immobilized on the surface of Fe_3O_4 directly. The magnetic orientation of Fe_3O_4 @noble metal nanocomposite and specifically capturing of ACE2 could achieve the select detection of SARS-CoV-2 in complex environment [21,22].

In this work, we present one high-sensitivity and point-of-care detection method (Scheme 1) for SARS-CoV-2 by developing a Fe_3O_4-Au nanocomposite modified with ACE2 to capture, enrich, and partially enhance the Raman signals for SARS-CoV-2, and detecting the virus transferred from the Fe_3O_4-Au-ACE2-virus composite by gold nanoneedles array SERS biosensor [21]. By optimizing the Fe_3O_4-Au nanocomposite, we obtained the magnetic SERS biosensor with ultrahigh sensitivity. More usefully, on-site detection of inactivated SARS-CoV-2 in the nasal and throat swabs with 100 copies/mL could also be achieved within 15 mins by portable Raman devices, which exhibited excellent point-of-care detection potential. What's more, support vector machine (SVM) was applied for classifying the contaminated swabs with 100% accuracy. Based on the magnetic SERS biosensor and SVM, the biosensor has the potential to screen and diagnose the SARS-CoV-2 in the current COVID-19 pandemic.

2. Experimental

2.1. materials and instruments

Iron (III) Chloride, Sodium acetate trihydrate, (3-Aminopropyl) trimethoxy silane (APTMS, 97%), Ammonia solution (GR, 25–28%), Gold chloride trihydrate, Sodium citrate dihydrate, sodium hydroxide, Tetrakis (hydroxymethyl) phosphonium chloride solution (THPC, 80% in water), Hydroxylamine solution (50% in water) were from Shanghai Aladdin Biochemical Technology Co., Ltd. Ethylene glycol was purchased from Sinopharm Chemical Reagent Co., Ltd. All the reagents were used directly without purification. SARS-CoV-2 pseudovirus were provided by Sanyou biopharmaceuticals Co., Ltd. The intact and inactivated SARS-CoV-2 viruses were provided by Anhui Provincial Center for Disease Control and Prevention. Heat inactivated process was employed for the inactivation of viruses, and the inactivated details were presented in the supporting information S1 [21,23,24]. The nasal / throat swabs and the disposable virus sampling tube which can maintain the integrity of the SARS-CoV-2 virus were purchased from BIOBASE BIODUSTRY(SHANDONG) CO., LTD.

The images of Fe_3O_4 were obtained by scanning electron microscopy (SEM, sigma300). Transmission electron microscopy (Talos F200X G2) was used to characterize the morphology and element mapping of Fe_3O_4-Au nanocomposite with an accelerating voltage of 200 kV. X-ray photoelectron spectroscopy (XPS, from Thermo Fisher Scientific) was employed to assess the chemical properties of Fe_3O_4-Au nanocomposite. The UV-Vis images were obtained by a PerkinElmer Ultraviolet visible spectrophotometer (Lambda 950). For the Raman spectra of Rhodamine 6 G (R6G) and pseudovirus in the lab, Renishaw inVia Reflex laser confocal micro-Raman spectrometer was used to acquire the Raman signals. And for the on-site detection of inactivated virus, the portable Raman spectrometer (from Shanghai Oceanhood opto-electronics Co., Ltd) was applied.

2.2. Preparation of Fe_3O_4-Au nanocomposite

Monodisperse Fe_3O_4 microspheres were synthesized according to a modified method proposed by Hong Deng [25]. The mixture of 0.6 g $FeCl_3$, 3 g CH_3COONa and 30 mL ethylene glycol was heated to 60 ℃ and stirred vigorously for 1 h, then the transparent solution was obtained. The prepared solution was poured into Teflon-lined stainless--steel autoclave and heated at 190 ℃ for 6 h. The black product was collected by the external magnetic field, cleaned with ethanol and deionized water (DI water) two times separately, and dried at 60 ℃ for 12 h.

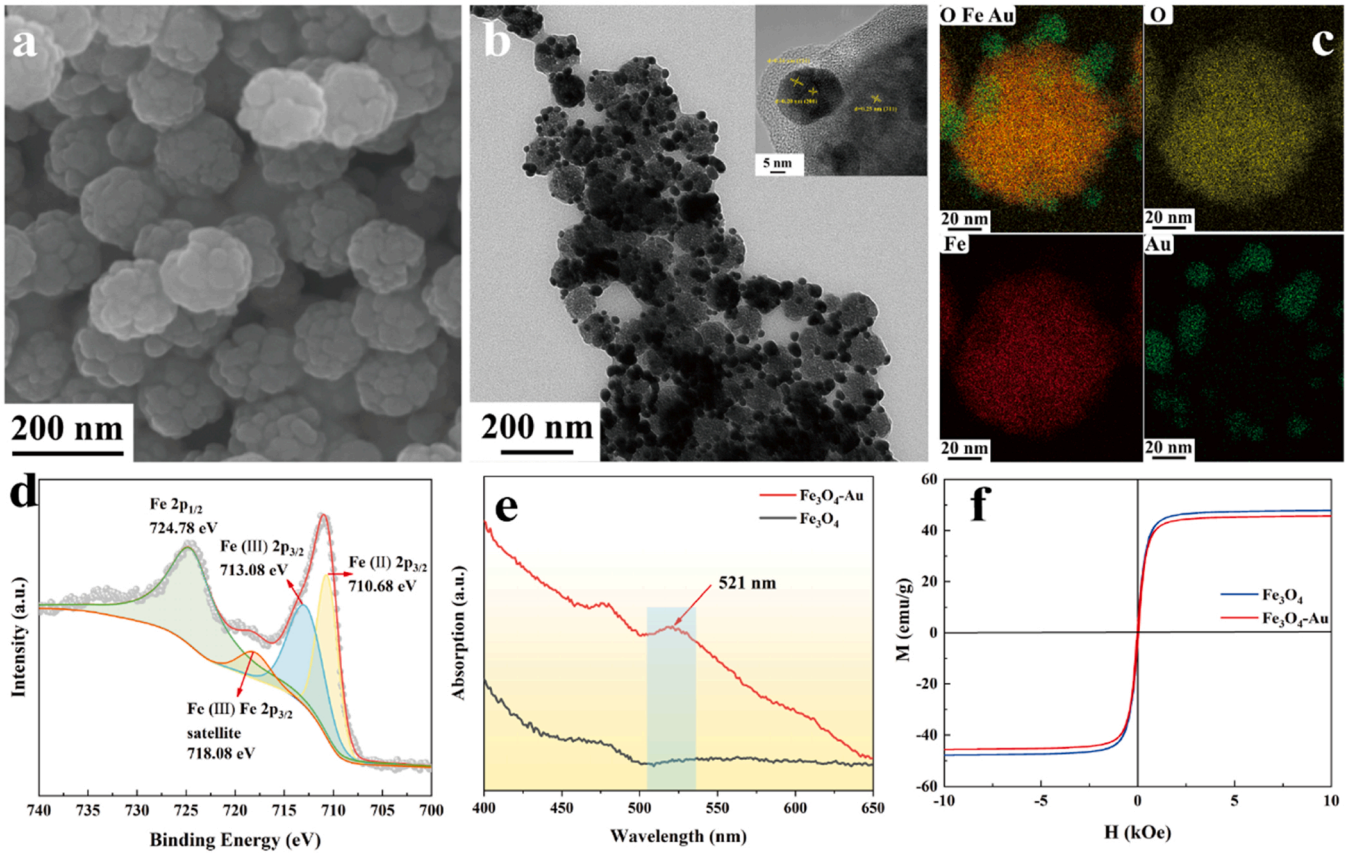

Fig. 1. Characterization of Fe_3O_4-Au nanocomposite. (a) The SEM image of Fe_3O_4 microsphere. (b) The TEM image of Fe_3O_4-Au nanocomposite. (c) The EDS mapping of Fe_3O_4-Au nanocomposite. (d) The XPS spectrum of Fe element in Fe_3O_4-Au nanocomposite. (e) The UV-Vis absorption spectra of Fe_3O_4 and Fe_3O_4-Au nanocomposite. (f) Magnetic hysteresis loops of Fe_3O_4 and Fe_3O_4-Au nanocomposite.

The Au nanoparticles were loaded on Fe_3O_4 microspheres by the modified method proposed by Zihao Li et al. [26,27]. The synthesis process of Fe_3O_4-Au was divided into three parts: functionalizing the Fe_3O_4 with the amino functional group, preparing the above 2 nm Au seeds and adsorbing of Au seeds, and growing the Au seeds [19,28,29]. Firstly, add 2 mL ammonia and 1 mL APTMs to the mixture of 40 mg Fe_3O_4, 40 mL DI water of and 80 mL absolute ethyl alcohol, and stir for 12 h mechanically. The product was collected by magnet, and cleaned by ethanol and deionized water. The next part was the synthesis of Au seeds, 1 mL THPC solution (12 μL THPC in 1 mL DI water) and 0.5 mL NaOH solution (1 M) were added into 45 mL DI water. The solution was stirred violently for 5 mins, and added 2 mL $HAuCl_4$ (27 mM) quickly. The prepared solution was stirred for 2 h at room temperature. Pour the solution contained Au seeds into the prepared Fe_3O_4-NH_2 and stir for 12 h. Then clean the Fe_3O_4-Au seeds with water. The ultimate step is the growth of Au seeds. Add 3 mL sodium citrate (1 wt%) and 1.5 mL $HAuCl_4$ (27 mM) to 50 mL Fe_3O_4-Au seeds solution. Then add 6 μL hydroxylamine (60 wt%) in above solution and stir for 6 h. Finally, collect the product by magnet and clean with DI water. The sizes ratio between Fe_3O_4 microspheres and Au nanoparticles is regulated to optimize the SERS performance by changing the stepwise growth times of Au nanoparticles from two to six times. The ultimate nanocomposites were dispersed in 50 mL DI water to be used.

2.3. Modification Fe_3O_4-Au with His-ACE2

Before detecting of SARS-CoV-2 pseudovirus and inactivated virus, the SERS-active substrate Fe_3O_4-Au nanocomposite should be modified with the specific protein to capture targets. Human His-ACE2 (0.35 mg/mL) was mixed with Fe_3O_4-Au nanocomposite and incubated for 2 h. After the combination between Fe_3O_4-Au nanocomposite and His-ACE2, it is necessary to wash the above product to remove the redundant ACE2.

2.4. SERS detection for pseudovirus and inactivated virus of SARS-CoV-2

For the detection of pseudovirus in the laboratory, 20 μL 2.76×10^5 copies/mL virus was diluted to the concentration gradient from 2.76×10^4 to 2.76×10^2 copies/mL, and mixed with 25 μL Fe_3O_4-Au-ACE2 thoroughly. Then acquire the Raman signals by the Confocal Raman Spectrometer with 785 nm near-IR laser source with the following parameters: 1 s acquisition time and 0.6 mW laser power.

For SARS-CoV-2 on-site test, taking inactivated virus detection in nasal swabs solution as an example. Firstly, mix 100 μL negative and positive nasal / throat swabs (1300 copies/mL to 60 copies/mL) with Fe_3O_4-Au-ACE2 thoroughly, then enrich the composite with external magnet and wash it by several times. The composite was deposited on Au nanoneedles array and dried (the preparation process of Au nanoneedles array was depicted in Supporting Information S2). Then detection was measured by portable Raman spectrometer (RMS 1000) with the following parameters: 785 nm laser source, 2 s acquisition time, and 100 mW laser power.

2.5. Support vector machine and date analysis

SVM models were trained using toolbox LIBSVM 3.24 for MATLAB [30]. The training accuracy of Linear kernels, Polynomial kernel and RFB kernel were verified through the cross-validation program, and finally the Linear kernel with the highest accuracy was selected. In our study, a total of 603 Raman shifts from 500 to 1800 cm^{-1} were chosen as the variables for SVM using MATLAB. The date matrix consisted of 200

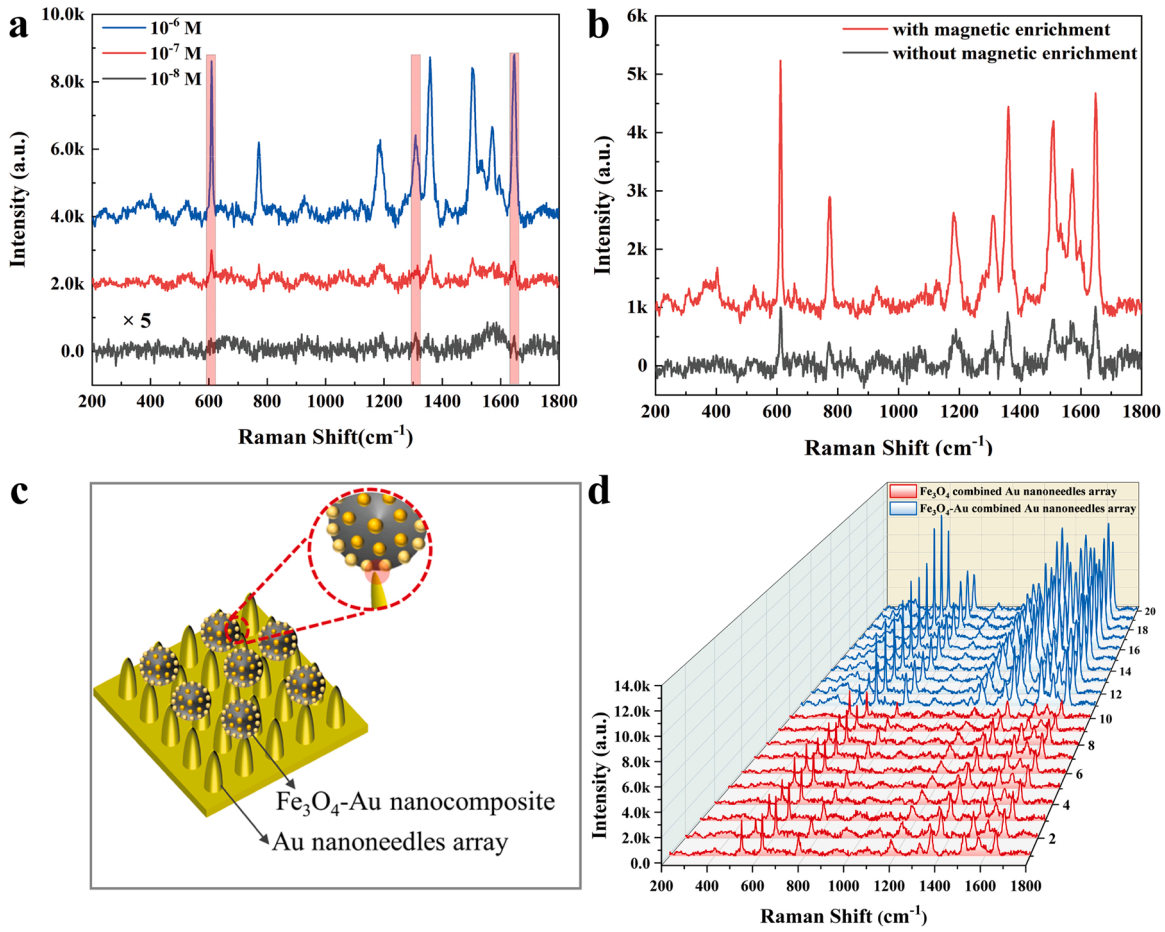

Fig. 2. The SERS performance of Fe_3O_4-Au nanocomposite. (a) The SERS spectra of R6G solutions with concentrations ranging from 10^{-6} M to 10^{-8} M (The "× 5" on the left side of the figure is the magnification of the Raman spectra under this scale). (b) The SERS spectra of 10^{-6} M R6G by Fe_3O_4-Au nanocomposite with magnetic enrichment (red line) and without magnetic enrichment (black line). (c) The schematic diagram of magnetic SERS biosensor structure which is Fe_3O_4-Au nanocomposite combined with Au nanoneedles array. (d) The Raman mapping image of 10^{-6} R6G based on Fe_3O_4 microspheres combined with Au nanoneedles array (red lines) and Fe_3O_4-Au nanocomposites combined with Au nanoneedles array (blue lines).

Raman spectra including 100 simulated nasal swabs and 100 simulated throat swabs, respectively. The raw data subtracts the mean value from the spectral intensity matrix after area normalization to obtain the mean-centered matrix, and used for subsequent multivariate analysis [31]. The mean-centered approach can eliminate the influence of intra-subject and/or inter-subject spectral variability on multivariate analysis. The built-in "SVM" function was used to get principal component coefficients, training set (60%), test set (40%) and hyperplane, etc.

In order to explain the SVM classification result, Principal Component Analysis (PCA) was used to discover the characteristics of Raman spectra of simulated nasal/throat swabs. Principal component (PCs) was obtained to capture the key Raman shifts of spectra from targets.

3. Results and discussion

3.1. Characterization of Fe_3O_4-Au nanocomposite

We prepared the Fe_3O_4-Au nanocomposite which Au nanoparticles (Au NPs) were loaded on the surface of Fe_3O_4 microspheres. Fig. 1 showed the morphology and properties of Fe_3O_4 and Fe_3O_4-Au nanocomposite. Fe_3O_4 microspheres were spherical and their sizes were about 150 nm with excellent monodisperse (Fig. 1(a)). In terms of the microstructure of Fe_3O_4 microsphere, it was constituted with many ultrafine Fe_3O_4 nanoparticles. As depicted in Fig. 1(b), the Au nanoparticles (above 20 nm) were loaded on the surface of Fe_3O_4 microspheres successfully. The insert in Fig. 1(b) was the HRTEM image of Fe_3O_4-Au nanocomposite. The crystal fringes with a spacing of 0.25 nm were ascribed to the (311) crystal plane of Fe_3O_4 microspheres. The twins in Au crystal can be observed, which were ascribed to the (111) and (200) crystal planes. The formation of Fe_3O_4-Au nanocomposite was attributed to the electrostatic interaction between positively charged amino functional groups and negatively charged colloidal Au.

Some convincing evidence could also prove the successful load of Au NPs on the Fe_3O_4 microspheres. Fig. 1(c) was the corresponding elemental mapping images, which exhibited the relative location between Au NPs and Fe_3O_4 microspheres. Fig. 1(d) showed the analysis of Fe 2p for Fe_3O_4-Au nanocomposite. The peaks located at 724.78 eV, 713.08 eV, and 710.68 eV were attributed to $2p_{1/2}$ and $2p_{3/2}$, respectively. And the appearance of the peak located at 718.08 eV indicated the formation of γ-Fe_2O_3, which was due to partial oxidation of Fe_3O_4 [32]. Fig. S1(a) and (b) were the XPS spectrum for Fe_3O_4-Au nanocomposite and high-resolution XPS spectrum of Au 4 f. XPS analysis demonstrated the successful preparation of expected Fe_3O_4-Au nanocomposite [33]. As shown in Fig. 1(e), the UV-Vis spectra of Fe_3O_4 and Fe_3O_4-Au nanocomposite showed the typical 521 nm absorption peak that was corresponding to the plasma resonance of Au NPs. XRD analysis can also prove the successful preparation of Fe_3O_4-Au nanocomposite (Fig. S1(c)). The XRD spectra of Fe_3O_4-Au nanocomposite (red line) appeared four additional peaks at 38.24°, 44.41°, 64.65°, and 77.57°, which were corresponding to the (111), (200), (220), (311) crystal face

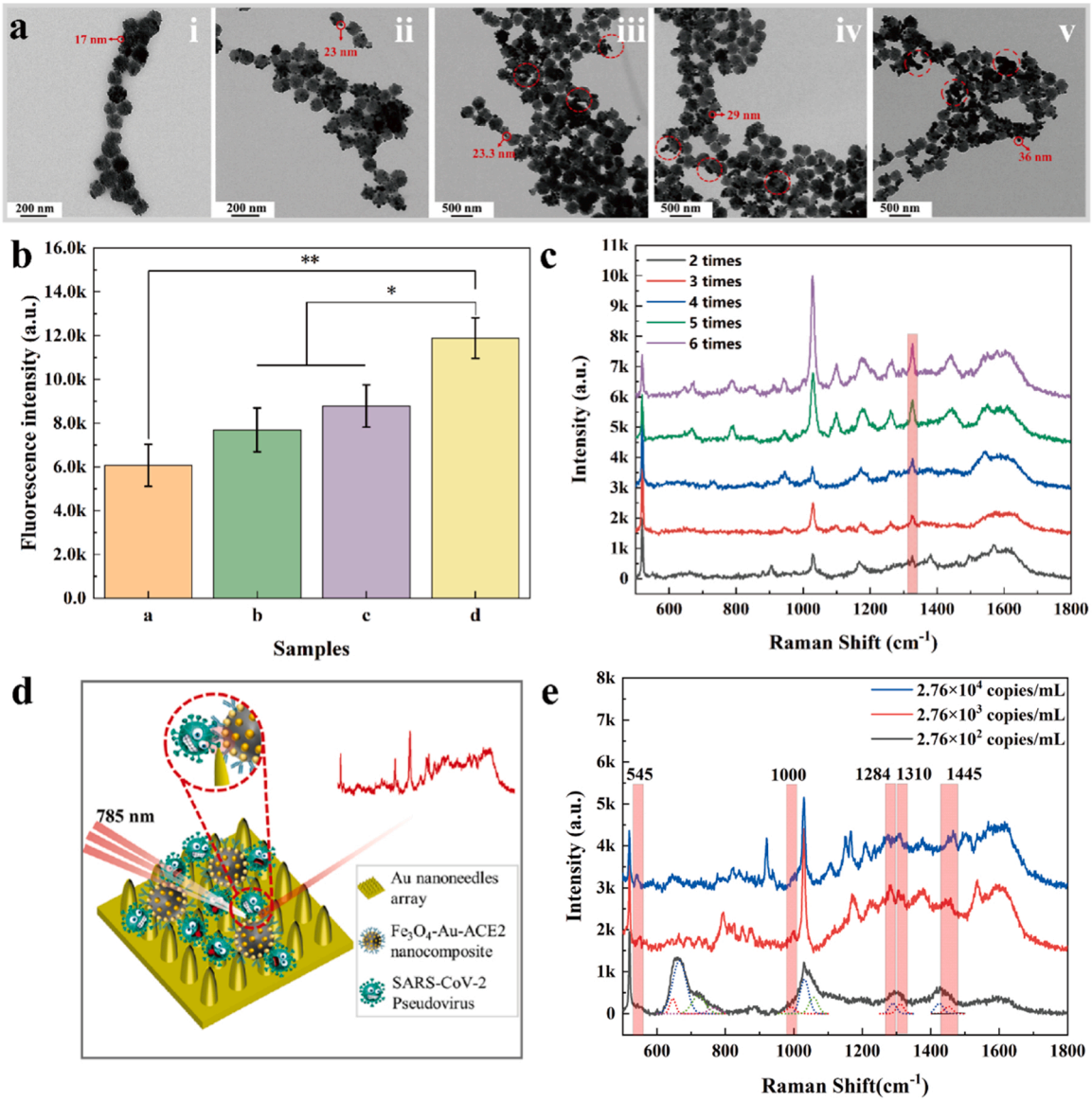

Fig. 3. The optimization of Fe_3O_4-Au nanocomposite and the detection of SARS-CoV-2 pseudovirus with the most optimal magnetic SERS biosensor. (a) the TEM images of Fe_3O_4-Au nanocomposite with different growth times from two times to six times (i-v). (b) The fluorescence intensity of four samples, letter a: Fe_3O_4-Au-FITC composite, letter b: Fe_3O_4-Au-ACE2-FITC composite, letter c: Fe_3O_4-Au-pseudovirus-FITC composite, letter d : Fe_3O_4-Au-ACE2-pseudovirus-FITC composite. (c) The SERS performance comparation of ACE2 based on magnetic SERS biosensor with different growth times of Au NPs. (d) The structure of magnetic SERS biosensor in detecting pseudovirus. (e) The Raman spectra of SARS-CoV-2 pseudovirus with different viral load from 2.76 × 10^4 copies/mL to 2.76 × 10^2 copies/mL, the solid line is the Raman spectra of pseudovirus and the dash line is the fitted Raman shift by Peakfit software.

of Au (JCPDS, card No.19–0629). We suggested that the Fe_3O_4-Au nanocomposite was prepared successfully.

As shown in Fig. 1(f), the magnetism of Fe_3O_4 microspheres and Fe_3O_4-Au nanocomposite were characterized by the magnetic hysteresis loop. The magnetic saturation (MS) values of Fe_3O_4 and Fe_3O_4-Au nanocomposite were around 47.83 emu/g and 45.567 emu/g, respectively. The reduction of MS values was tiny, proving that the magnetic property was still excellent after loading Au NPs. And the hysteresis loop wasn't detected, indicating that Fe_3O_4-Au nanocomposite was superparamagnetic at room temperature. The magnetic property of Fe_3O_4-Au was favorable to separate the target substance from the complex environment. In conclusion, the above experimental results indicated the successful preparation of the Fe_3O_4-Au nanocomposite.

3.2. The SERS performance of Fe_3O_4-Au nanocomposite and magnetic SERS biosensor

In a typical SERS analysis, the enhancement factor (EF) and limit of detection (LOD) are used to evaluate the SERS performance. R6G aqueous solution of different concentrations (from 10^{-6} M to 10^{-8} M) was selected to characterize the SERS performance. The resonance absorption peak of R6G is located at 524 nm. So, the Raman signals are collected with 532 nm laser source for producing resonance enhancement effect [34]. As shown in Fig. 2(a), the characteristic band around 611 cm^{-1} was corresponding to the C-C-C ring in-plane. The bands at 771 and 1184 cm^{-1} were attributed to C-H out-of-plane and C-H in-plane bending vibrations, respectively. And the bands at 1360 cm^{-1}, 1505 cm^{-1}, 1570 cm^{-1}, and 1646 cm^{-1} were assigned to the symmetric modes of in-plane C-C stretching and C-O-C stretching vibrations [35]. The nanocomposite possessed excellent sensitivity with the LOD of 10^{-8}

M, and EF was 1.4×10^8 for 10^{-6} M R6G with the irradiation laser of 532 nm according to the equation of SERS enhancement factor: $EF = \frac{I_{SERS}/N_{SERS}}{I_{Raman}/N_{Raman}}$ (the detail of calculation is described in the Supporting Information S3) [36,37]. We assessed the magnetic enrichment capacity of Fe_3O_4-Au nanocomposite by comparing the direct SERS detection and SERS enrichment-detection. Direct SERS detection referred that the Fe_3O_4-Au nanocomposite was deposited and dried on silica glass, and then R6G were deposited on the Fe_3O_4-Au nanocomposite. SERS enrichment-detection referred that the mixture of Fe_3O_4-Au nanocomposite and R6G was enriched by external magnet, and deposited on silica glass for SERS detection [38]. The SERS enrichment-detection of 10^{-6} M R6G with the magnetic field is around four times better than those without magnetic field as shown in Fig. 2(b). The enrichment effect with the external magnet was in favor of enhancing SERS performance for Fe_3O_4-Au nanocomposite.

In order to increase the optical enhancement performance of Fe_3O_4-Au nanocomposite, the nanocomposite captured target molecules was deposited on Au nanoneedles array for detection. The more details of Au nanoneedles array (GNA) can refer to our published literature [21,39]. The nanoneedles with a 15 nm apex diameter are arranged with an oblique angle of 45° to Si substrates. The "lighting-rod" effect induced by sharp tips and electromagnetic field coupling caused by the special nanostructure GNA synergistically enhance the SERS effect with the EF of 10^9 for R6G. The magnetic SERS biosensor was constituted with two parts: Fe_3O_4-Au nanocomposite and Au needles array as depicted in Fig. 2(c). The SERS enhancement of Fe_3O_4 combined with GNA and Fe_3O_4-Au nanocomposite combined with GNA were compared in Fig. 2 (d). The results indicated that Au NPs on the surface of Fe_3O_4 microspheres played a significant role in the SERS enhancement. Therefore, we concluded that the enhancement mechanism for our magnetic SERS biosensor was ascribed to local surface plasmon resonance produced by Au nanoparticles coupling Au nanoneedles array.

3.3. Optimization of Fe_3O_4-Au nanocomposite for immobilizing ACE2 and ultra-sensitive detection of SARS-CoV-2 pseudovirus

We prepared the Fe_3O_4-Au nanocomposite with different size ratios between Fe_3O_4 microspheres and Au NPs by adjusting the stepwise growth times of Au NPs. The in-situ stepwise growth of Au NPs on the Fe_3O_4 microspheres was achieved by the iterative reduction process from 2 times to 6 times with NH_2OH [40]. As shown in Fig. 3(a), along with the increasing stepwise growth times of Au NPs, the size of Au NPs would increase and the load density of Au NPs would decrease. The target of optimization was to obtain the nanocomposite which could immobilize ACE2 as many as possible. ACE2 played a significant role in SARS-CoV-2 detection with our magnetic SERS biosensor, a series of fluorescence tests were implemented to prove the importance of ACE2. Polypeptide labelled 5-FITC (LVMGLNVWLRYSK(5-FITC), denoted as FITC) could recognize SARS-CoV-2 spike protein specifically, which was applied to combined with pseudovirus and provide fluorescence signals [41]. The fluorescence intensity of Fe_3O_4-Au-ACE2-pesudovirus-FITC composite is higher than the other control groups (Fe_3O_4-Au-pesudovirus-FITC composite, Fe_3O_4-Au-ACE2-FITC composite, Fe_3O_4-Au-FITC composite) as shown in Fig. 3(b). We suggested that more ACE2 on the surface of Fe_3O_4-Au nanocomposite was beneficial to detect SARS-CoV-2.

Fig. 3(c) was the SERS spectra of ACE2 (0.35 mg/mL) assembled onto magnetic SERS biosensor with different stepwise growth times of Au NPs. Along with the increasing of times, more peaks appeared and the intensity of the Raman band at 1324 cm^{-1} was stronger. The Fe_3O_4-Au nanocomposite with 5 times or 6 times growth presented the most optimal performance and the strongest Raman signal intensity. In our work, ACE2 served as a "hunter" was applied to capture the target virus due to the affinity between ACE2 and SARS-CoV-2 spike protein [20]. More ACE2 molecules would capture more target molecules and be in favor of the virus detection. Therefore, we preferred to develop the magnetic Fe_3O_4-Au nanocomposite that could graft more ACE2 and exhibit outstanding enhanced optical performance. The Raman intensity was proportional to the quantity of analyte normally, so the Fe_3O_4-Au nanocomposite of 5 times or 6 times stepwise growth was the best magnetic SERS substrate for SERS detection. However, compared to the Au NPs grown 5 times, 6 times growth would cause severe agglomeration and be more time-consuming. Considering cost-effectiveness, we chose the Fe_3O_4-Au nanocomposite with 5 times stepwise growth to be used.

The difference in SERS performance caused our interest to explore the mechanism for the above different SERS enhancement of ACE2. We attributed the phenomenon to two reasons which were the load density and size of Au NPs [42]. The combination between His-ACE2 and Fe_3O_4-Au nanocomposite is attributed to the electrostatic attraction between Fe_3O_4 microspheres and Histidine, so load density of Au NPs is essential to the attachment of ACE2. The load density of Au NPs should maintain an appropriate value which is beneficial for combining ACE2 molecules and enhancing SERS signals. Along with the increasing growth times of Au NPs, the load density of Au NPs was gradually decreasing, and the exposed area of Fe_3O_4 was gradually increasing as shown in Fig. 3(a). Correspondingly, the SERS performance was better along the increasing area of Fe_3O_4 microsphere as shown in Fig. 3(c). The size of Au NPs also had greatly influenced the SERS performance of magnetic SERS biosensor. Along with increasing the reduction time, the size of Au NPs was bigger. The increasing size of Au NPs would cause red-shift of surface plasmon resonance, which was more close to excitation wavelength (785 nm) [40]. The increase of size tended to produce stronger electromagnetic enhancement and obtained more excellent SERS performance.

After optimizing the Fe_3O_4-Au nanocomposite, the nanocomposite combined Au nanoneedles array was applied to detect SARS-CoV-2. Before on-site detection for our magnetic SERS biosensor, the sensitivity for SARS-CoV-2 detection was necessary to be accessed. Therefore, its pseudovirus model was detected directly with the magnetic SERS biosensor in the lab by the confocal micro-Raman spectrometer at 785 nm laser source, the process was shown schematically in Fig. 3(d). The Raman spectra of pseudovirus with different viral loads (2.76×10^4-2.76×10^2 copies/mL) were illustrated in Fig. 3(e), the solid line was the Raman signal acquired by the confocal micro-Raman spectrometer and the dashed line was fitted Raman peaks by PeakFit software. The Raman shift would change slightly and the Raman peak would broaden for the spectra of SARS-CoV-2 pseudovirus because of the orientation of molecule absorption for macromolecules [43]. Hence, we deconvoluted the peaks into individual components and acquired a more accurate analysis of the virus with PeakFit software [44].

The magnetic SERS biosensor possessed ultrahigh sensitivity for SARS-CoV-2 pseudovirus, with the LOD of 276 copies/mL. We could observe five characteristic peaks at 545 cm^{-1}, 1000 cm^{-1}, 1284 cm^{-1}, 1310 cm^{-1}, 1445 cm^{-1}. The band around 545 cm^{-1} assigns to S-S stretching[45,46]. The peak located at 1000 cm^{-1} is attributed to Phenylalanine ring mode, the Raman shift around 1284 cm^{-1} is corresponding to phosphodiester groups in nucleic acids, the Raman band at 1310 cm^{-1} is primarily related to Amide III (α-helix structure)[44,47]. Raman shift around 1445 cm^{-1} is responsible for the stretching vibration mode of Amino acid [48]. The magnetic SERS biosensor with ultrahigh sensitivity for detecting pseudovirus could further be applied for the on-site detection of SARS-CoV-2 in nasal and throat swabs.

3.4. Identification of SARS-CoV-2 from nasal and throat swabs

On-site screening of SARS-CoV-2 is an essential capability for the SERS-based diagnostic tools. The magnetic SERS biosensor can separate the target analyte from the complicated liquid environment by external magnetic field directly and simplify the detection process. Compared to the label-SERS biosensor, the direct label-free SERS biosensor is the

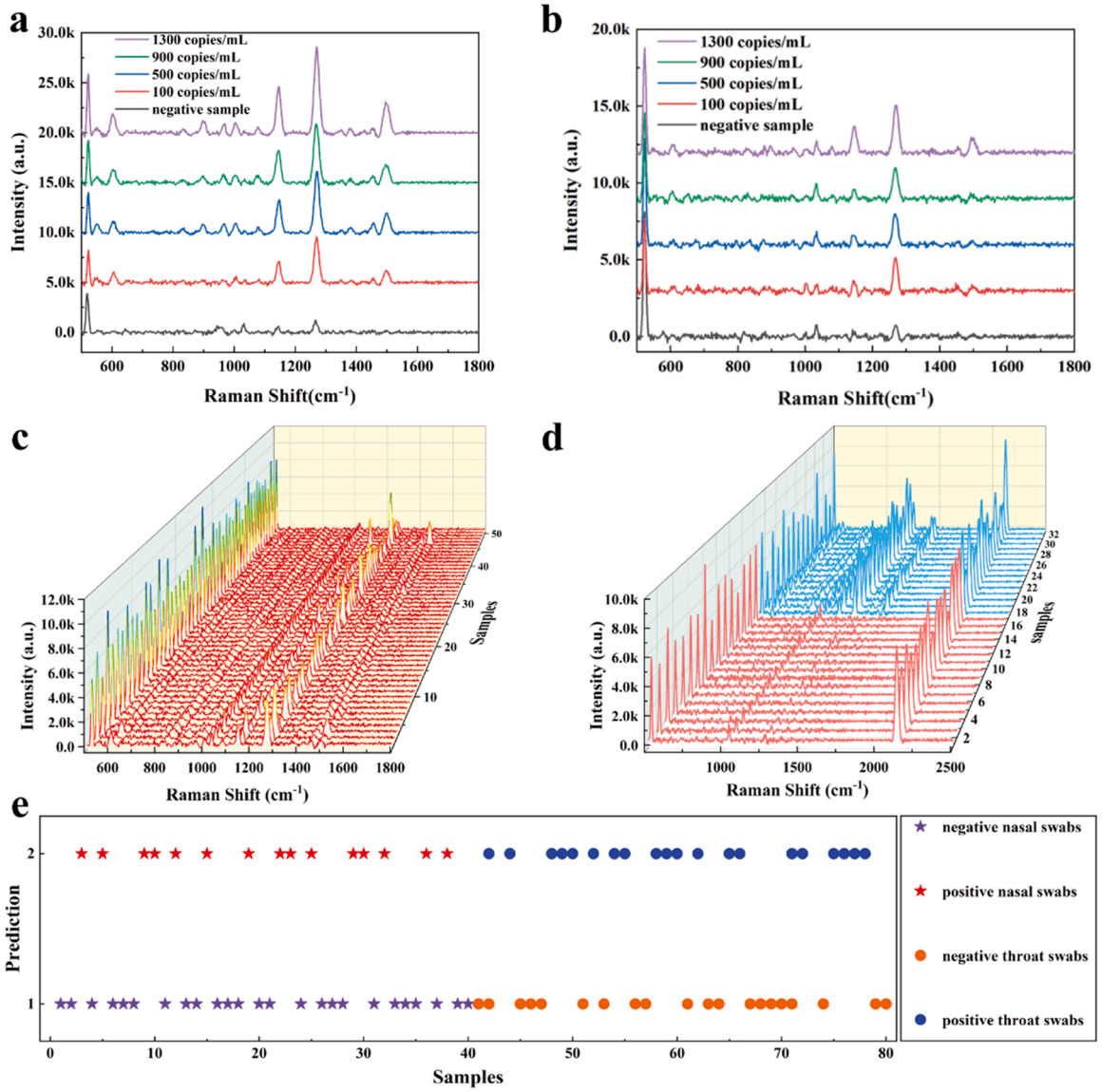

Fig. 4. The SERS detection of simulated nasal / throat swabs and classification of nasal / throat swabs. (a) The Raman spectra of simulated nasal swabs with different viral loads from 1300 copies/mL to 100 copies/mL. (b) The Raman spectra of simulated throat swabs with different viral loads from 1300 copies/mL to 100 copies/mL. (c) The mapping of Raman spectra for simulated nasal swabs with 60 copies/mL viral loads. (d) The mapping of Raman spectra for simulated nasal swabs (100 copies/mL, bule lines) and negative throat swabs (red lines). (e) the predicted model by SVM linear kernel function for simulated throat and nasal swab (100 copies/mL). Value 1 is a prediction as positive swabs solution and value 2 is a prediction as negative swabs solution.

simplest way to detect targets [49]. For estimating the specificity and accuracy of the magnetic SERS biosensor, the direct detection of the SARS-CoV-2 virus was performed by as-prepared Fe_3O_4-Au-ACE2 nanocomposite combined with GNA. To ensure the security for experimenters, we manipulated the detection process with simulated samples, which mixed inactivated SARS-CoV-2 virus and nasal and throat swabs of a healthy experimenter.

Fig. 4(a) and (b) were the Raman spectra of simulated nasal and throat swabs with different viral loads from 1300 copies/mL to 100 copies/mL for positive nasal / throat swabs with portable Raman spectrometer. As shown in Fig. 4(c), the intensity of Raman spectra became inconsistent and some even were equal to Raman intensity of negative samples when the viral loads were down to 66 copies/mL. These results indicated that the magnetic SERS biosensor possessed high sensitivity with the LOD of 66 copies/mL (the corresponding Raman spectra of contaminated throat swabs were shown in Fig. S3(a)). However, we need more time to find the Raman signals because of the uneven distribution of virus. Therefore, the magnetic SERS biosensor is more suitable for detecting SARS-CoV-2 virus with 100 copies/mL and over viral loads. The whole detection process only took 15 min. Thus, the biosensor with high sensitivity and short detection time is practical for on-site detection of SARS-CoV-2 virus.

From the perspective of Raman spectra, the characteristic Raman shifts of simulated positive and negative nasal / throat swabs (with 100 copies/mL) were similar as shown in Fig. 4(d) and Fig. S3(b). The obvious distinction was the Raman intensity, that is, the Raman intensity of simulated positive nasal and throat swabs was higher than those of negative samples. We concluded that the difference of Raman intensity was attributed to the ACE2 structure deformation. The N- and C- terminal domains would move closer after binding SARS-CoV-2 spike protein, the deformation might cause ACE2 closer to the SERS-active site and increase the SERS intensity [50]. However, we can't discriminate the samples with virus rapidly only according to the difference of intensity sometimes. Therefore, in order to deal with the high similarity of Raman spectra between ACE2 and SARS-CoV-2 virus, SVM was applied to establish classification model which aimed to classify the positive

Table 1
SVM classification of simulated nasal and throat swabs with linear kernel function.

		Training set				Test set			
			Original class				Original class	
			Positive	Negative			Positive	Negative
Nasal swab	Predict class	Positive	25	0	Predict class	Positive	25	0
		Negative	0	35		Negative	0	15
			Accuracy: 100%				Accuracy: 100%	
			Original class				Original class	
			Positive	Negative			Positive	Negative
Throat swab	Predict class	Positive	30	0	Predict class	Positive	20	0
		Negative	0	30		Negative	0	20
			Accuracy: 100%				Accuracy: 100%	

samples from unknown samples. And PAC was applied to discover the characteristics of Raman spectra of simulated nasal / throat swabs. As shown in Fig. S4, PCA loading plots were performed by with the eigenvectors of covariance matrix and the Raman spectra was projected onto the PCA score space. The measured SERS spectra were classified by SVM classification models with linear function, polynomial function, and Gaussian radial basis function (RBF) [31]. As shown in Fig. S5, the parameters were optimized by cross validation of training set data. The maximum diagnostic accuracy with 100%, 98.3%, and 55% were obtained for linear kernel function, polynomial kernel function, and RBF, respectively. According to the result of cross validation, we selected the linear kernel function as the algorithm model to establish classification model.

The date matrix consisted of 200 Raman spectra by 604 variables, including 100 simulated nasal swabs and 100 simulated throat swabs, respectively. The Raman shifts from 500 to 1800 cm^{-1} were defined as the region of interest (ROI), because reliable identification of protein located at this spectral region [44]. The spectra of simulated nasal swabs were randomly organized and divided into two groups: training sets and test sets, composed of 60 and 40 samples, respectively. Among, training sets consisted of 25 positive samples and 35 negative samples. For simulated throat swabs, 30 positive samples and 30 negative samples were trained to predict 40 unknown samples. Fig. 4(e) illustrated the classification results of the throat and nasal swabs, the star pattern and circle pattern with two colors represented the positive and negative nasal/throat samples, respectively. The SVM algorithm could distinguish the different samples successfully without misclassification. The confusion matrix for the training set and test set for throat / nasal swabs was listed in Table 1. The model possessed excellent outcomes with 100% accuracy both for two types of simulated samples. SERS spectra of contaminated viral samples can be identified based on SVM model rapidly, and the magnetic SERS biosensor combined with the SVM possesses the universality for two kinds of samples (throat swabs and nasal swabs). The rapid and ultra-sensitive magnetic SERS biosensor possessed high potential in the on-site detection of SARS-CoV-2.

4. Conclusion

We have developed one high-sensitivity and point-of-care detection method for SARS-CoV-2 based on Fe_3O_4-Au nanocomposite and Au nanoneedles array SERS biosensors. Fe_3O_4-Au nanocomposite was employed to capture and enrich virus, which was partially responsible for enhancing the Raman signals for SARS-CoV-2. By adjusting the growth times of Au NPs on the surface of Fe_3O_4-Au nanocomposite, the most optimal magnetic SERS biosensor with high sensitivity was obtained. More importantly, this method based on magnetic SERS biosensor could detect the contaminated viral samples with 100 copies/mL during 15 mins by portable Raman spectrometer. SVM was employed to classify the positive samples with the accuracy of 100%. With excellent sensitivity and accuracy, the magnetic SERS biosensor has great potential to restrain the COVID-19 epidemic.

CRediT authorship contribution statement

Yanyan Li: Conceptualization, Investigation, Writing – original draft, Methodology. **Chenglong Lin**: Software, Formal analysis, Investigation. **Yusi Peng**: Methodology, Validation, Writing – original draft. **Jun He**: Resources. **Yong Yang**: Conceptualization, Supervision, Writing – review & editing.

Declaration of Competing Interest

The authors declare that they have no known competing financial interests or personal relationships that could have appeared to influence the work reported in this paper.

Acknowledgement

This work is supported by the finical support of the National Natural Science Foundation of China (No. 52172167) and National Key Research and Development Project (No. 2021YFE011305), and authors also gratefully acknowledge financial support from the Key Research and Development Plan of Anhui Province (No. 202104a07020032).

Appendix A. Supporting information

Supplementary data associated with this article can be found in the online version at doi:10.1016/j.snb.2022.131974.

References

[1] J. Sitjar, J.D. Liao, H. Lee, H.P. Tsai, J.R. Wang, P.Y. Liu, Challenges of SERS technology as a non-nucleic acid or -antigen detection method for SARS-CoV-2 virus and its variants, Biosens. Bioelectron. 181 (2021), 113153.
[2] Z. Zhang, Z. Tang, N. Farokhzad, T. Chen, W. Tao, Sensitive, rapid, low-cost, and multiplexed COVID-19 monitoring by the wireless telemedicine platform, Matter 3 (2020) 1818–1820.
[3] R.M. Torrente-Rodriguez, H. Lukas, J. Tu, J. Min, Y. Yang, C. Xu, et al., SARS-CoV-2 rapidplex: a graphene-based multiplexed telemedicine platform for rapid and low-cost COVID-19 diagnosis and monitoring, Matter 3 (2020) 1981–1998.
[4] W. Chen, B. Cai, Z. Geng, F. Chen, Z. Wang, L. Wang, et al., Reducing false negatives in COVID-19 testing by using microneedle-based oropharyngeal swabs, Matter 3 (2020) 1589–1600.
[5] F. Cui, H.S. Zhou, Diagnostic methods and potential portable biosensors for coronavirus disease 2019, Biosens. Bioelectron. 165 (2020) 112349.
[6] D. Lin, L. Liu, M. Zhang, Y. Hu, Q. Yang, J. Guo, et al., Evaluations of the serological test in the diagnosis of 2019 novel coronavirus (SARS-CoV-2) infections during the COVID-19 outbreak, Eur. J. Clin. Microbiol. Infect. Dis. 39 (2020) 2271–2277.
[7] P.B. van Kasteren, B. van der Veer, S. van den Brink, L. Wijsman, J. de Jonge, A. van den Brandt, et al., Comparison of seven commercial RT-PCR diagnostic kits for COVID-19, J. Clin. Virol. 128 (2020), 104412.
[8] Z.G. Wu, H.Y. Zheng, J. Gu, F. Li, R.L. Lv, Y.Y. Deng, et al., Effects of different temperature and time durations of virus inactivation on results of real-time fluorescence PCR testing of COVID-19 viruses, Curr. Med. Sci. 40 (2020) 614–617.
[9] M Zhang, X Li, J Pan, Y Zhang, L Zhang, C Wang, et al., Ultrasensitive detection of SARS-CoV-2 spike protein in untreated saliva using SERS-based biosensor, Biosens. Bioelectron 190 (2021) 113421.
[10] E. Callaway, Delta coronavirus variant: scientists brace for impact, Nature 595 (2021) 17–18.

[11] C. Wang, M. Liu, Z. Wang, S. Li, Y. Deng, N. He, Point-of-care diagnostics for infectious diseases: From methods to devices, Nano Today 37 (2021), 101092.
[12] H. Chen, A. Das, L. Bi, N. Choi, J.I. Moon, Y. Wu, et al., Recent advances in surface-enhanced Raman scattering-based microdevices for point-of-care diagnosis of viruses and bacteria, Nanoscale 12 (2020) 21560–21570.
[13] K. Xu, R. Zhou, K. Takei, M. Hong, Toward flexible surface-enhanced Raman scattering (SERS) sensors for point-of-care diagnostics, Adv. Sci. 6 (2019), 1900925.
[14] H. Liu, E. Dai, R. Xiao, Z. Zhou, M. Zhang, Z. Bai, et al., Development of a SERS-based lateral flow immunoassay for rapid and ultra-sensitive detection of anti-SARS-CoV-2 IgM/IgG in clinical samples, Sens. Actuators B Chem. 329 (2021), 129196.
[15] S. Chen, L. Meng, L. Wang, X. Huang, S. Ali, X. Chen, et al., SERS-based lateral flow immunoassay for sensitive and simultaneous detection of anti-SARS-CoV-2 IgM and IgG antibodies by using gap-enhanced Raman nanotags, Sens. Actuators B Chem. 348 (2021), 130706.
[16] M. Taniguchi, S. Minami, C. Ono, R. Hamajima, A. Morimura, S. Hamaguchi, et al., Combining machine learning and nanopore construction creates an artificial intelligence nanopore for coronavirus detection, Nat. Commun. 12 (2021) 3726.
[17] Y. Sun, L. Xu, F. Zhang, Z. Song, Y. Hu, Y. Ji, et al., A promising magnetic SERS immunosensor for sensitive detection of avian influenza virus, Biosens. Bioelectron. 89 (2017) 906–912.
[18] T. Yang, X. Guo, Y. Wu, H. Wang, S. Fu, Y. Wen, et al., Facile and label-free detection of lung cancer biomarker in urine by magnetically assisted surface-enhanced Raman scattering, ACS Appl. Mater. Interfaces 6 (2014) 20985–20993.
[19] C. Wang, C. Wang, X. Wang, K. Wang, Y. Zhu, Z. Rong, et al., Magnetic SERS strip for sensitive and simultaneous detection of respiratory viruses, ACS Appl. Mater. Interfaces 11 (2019) 19495–19505.
[20] S. Preziuso, Severe acute respiratory syndrome coronavirus 2 (SARS-CoV-2) exhibits high predicted binding affinity to ACE2 from lagomorphs (Rabbits and Pikas), Animals 10 (2020) 1460.
[21] Y. Yang, Y. Peng, C. Lin, L. Long, J. Hu, J. He, et al., Human ACE2-functionalized gold "virus-trap" nanostructures for accurate capture of SARS-CoV-2 and single-virus SERS detection, Nanomicro Lett. 13 (2021) 109.
[22] D. Zhang, X. Zhang, R. Ma, S. Deng, X. Wang, X. Wang, et al., Ultra-fast and onsite interrogation of severe acute respiratory syndrome coronavirus 2 (SARS-CoV-2) in waters via surface enhanced Raman scattering (SERS), Water Res. 200 (2021), 117243.
[23] E.I. Patterson, T. Prince, E.R. Anderson, A. Casas-Sanchez, S.L. Smith, C. Cansado-Utrilla, et al., Methods of inactivation of SARS-CoV-2 for downstream biological assays, J. Infect. Dis. 222 (2020) 1462–1467.
[24] Y. Peng, C. Lin, Y. Li, Y. Gao, J. Wang, J. He, et al., Identifying infectiousness of SARS-CoV-2 by ultra-sensitive SnS2 SERS biosensors with capillary effect, Matter 5 (2022) 694–709.
[25] H. Deng, X. Li, Q. Peng, X. Wang, J. Chen, Y. Li, Monodisperse magnetic single-crystal ferrite microspheres, Angew. Chem. Int. Ed. Engl. 44 (2005) 2782–2785.
[26] Z.H. Li, J.H. Bai, X. Zhang, J.M. Lv, C.S. Fan, Y.M. Zhao, et al., Facile synthesis of Au nanoparticle-coated Fe3O4 magnetic composite nanospheres and their application in SERS detection of malachite green, Spectrochim. Acta A Mol. Biomol. Spectrosc. 241 (2020), 118532.
[27] K.R. Brown, Seeding of colloidal Au nanoparticle solutions. 2. Improved control of particle size and shape, ChemMater 12 (2000) 306–313.
[28] G. Ding, S. Xie, Y. Zhu, Y. Liu, L. Wang, F. Xu, Graphene oxide wrapped Fe_3O_4@Au nanohybrid as SERS substrate for aromatic dye detection, Sens. Actuators B: Chem. 221 (2015) 1084–1093.
[29] L. Song, N. Zhao, F.-J. Xu, Hydroxyl-rich polycation brushed multifunctional rare-earth-gold core-shell nanorods for versatile therapy platforms, Adv. Funct. Mater. 27 (2017) 1701255.
[30] C.C. Chang, C.J. Lin, LIBSVM: a library for support vector machines, ACM Trans. Intell. Syst. Technol. 2 (2011) 1–27.
[31] R. Dong, S. Weng, L. Yang, J. Liu, Detection and direct readout of drugs in human urine using dynamic surface-enhanced Raman spectroscopy and support vector machines, Anal. Chem. 87 (2015) 2937–2944.
[32] L.T. Zhang, P. Li, W.B. Mi, E.Y. Jiang, H.L. Bai, Positive and negative magnetoresistance in Fe_3O_4-based heterostructures, J. Magn. Magn. Mater. 324 (2012) 3731–3736.
[33] C. Li, J. Zhao, X. Yan, Y. Gu, W. Liu, L. Tang, et al., Tremella-like graphene-Au composites used for amperometric determination of dopamine, Analyst 140 (2015) 1913–1920.
[34] H.Y.W.Y.Q. Wang, S. Ma, X.J. Li, Surface-enhanced Raman scattering of rhodamine 6G and crystal violet co-adsorbed on Ag/Si-NPA, Chem. J. Chin. Univ. 33 (2012) 1306–1311.
[35] H. Li, X. Yue, N. Gao, J. Tang, X. Lv, J. Hou, Microwave method synthesis of magnetic ionic liquid/gold nanoparticles as ultrasensitive SERS substrates for trace clopidol detection, Anal. Bioanal. Chem. 412 (2020) 3063–3071.
[36] L. Yang, Y. Peng, Y. Yang, J. Liu, H. Huang, B. Yu, et al., A novel ultra-sensitive semiconductor SERS substrate boosted by the coupled resonance effect, Adv. Sci. 6 (2019), 1900310.
[37] Y. Peng, C. Lin, M. Tang, L. Yang, Y. Yang, J. Liu, et al., Niobium pentoxide ultra-thin nanosheets: a photocatalytic degradation and recyclable surface-enhanced Raman scattering substrate, Appl. Surf. Sci. 509 (2020) 145376.
[38] Y. Ye, J. Chen, Q. Ding, D. Lin, R. Dong, L. Yang, et al., Sea-urchin-like Fe3O4@C@Ag particles: an efficient SERS substrate for detection of organic pollutants, Nanoscale 5 (2013) 5887–5895.
[39] Y. Yang, M. Tanemura, Z. Huang, D. Jiang, Z.Y. Li, Y.P. Huang, et al., Aligned gold nanoneedle arrays for surface-enhanced Raman scattering, Nanotechnology 21 (2010), 325701.
[40] D.G.W. Kenneth, R. Brown, Michael J. Natan, Seeding of colloidal Au nanoparticle solutions. 2. Improved control of particle size and shape, Chem. Mater. 12 (2000) 306–313.
[41] S. Pomplun, M. Jbara, A.J. Quartararo, G. Zhang, J.S. Brown, Y.C. Lee, et al., De Novo discovery of high-affinity peptide binders for the SARS-CoV-2 spike protein, ACS Cent. Sci. 7 (2021) 156–163.
[42] X. Zhang, Y. Zhu, X. Yang, Y. Zhou, Y. Yao, C. Li, Multifunctional Fe_3O_4@TiO_2@Au magnetic microspheres as recyclable substrates for surface-enhanced Raman scattering, Nanoscale 6 (2014) 5971–5979.
[43] N. Feliu, M. Hassan, E. Garcia Rico, D. Cui, W. Parak, R. Alvarez-Puebla, SERS quantification and characterization of proteins and other biomolecules, Langmuir 33 (2017) 9711–9730.
[44] J.E. Sanchez, S.A. Jaramillo, E. Settles, J.J. Velazquez Salazar, A. Lehr, J. Gonzalez, et al., Detection of SARS-CoV-2 and its S and N proteins using surface enhanced Raman spectroscopy, RSC Adv. 11 (2021) 25788–25794.
[45] P.B.D. Silva, J.R.D. Silva, M.C. Rodrigues, J.A. Vieira, I.A. Andrade, T. Nagata, et al., Detection of SARS-CoV-2 virus via dynamic light scattering using antibody-gold nanoparticle bioconjugates against viral spike protein, Talanta 243 (2022), 123355.
[46] Z. Zhang, D. Li, X. Wang, Y. Wang, J. Lin, S. Jiang, et al., Rapid detection of viruses: based on silver nanoparticles modified with bromine ions and acetonitrile, Chem. Eng. J. 438 (2022), 135589.
[47] J. Huang, J. Wen, M. Zhou, S. Ni, W. Le, G. Chen, et al., On-site detection of SARS-CoV-2 antigen by deep learning-based surface-enhanced Raman spectroscopy and its biochemical foundations, Anal. Chem. 93 (2021) 9174–9182.
[48] Y. Yang, Y. Peng, C. Lin, L. Long, J. Hu, J. He, et al., Human ACE2-functionalized gold "virus-trap" nanostructures for accurate capture of SARS-CoV-2 and single-virus SERS detection, Nano-Micro Lett. 13 (2021) 109.
[49] P. Matteini, M. Cottat, F. Tavanti, E. Panfilova, M. Scuderi, G. Nicotra, et al., Site-selective surface-enhanced Raman detection of proteins, ACS Nano 11 (2017) 918–926.
[50] J. Lu, P.D. Sun, High affinity binding of SARS-CoV-2 spike protein enhances ACE2 carboxypeptidase activity, J. Biol. Chem. 295 (2020) 18579–18588.

Yanyan Li is a Ph.D. candidate under the guidance of professor Yang at Shanghai Institute of Ceramics, Chinese Academy of Sciences. Her work focuses on the development of magnetic SERS substrate and biosensors for the on-site detection of virus.

Chenglong Lin is a Ph.D. candidate at Shanghai Institute of Ceramics, Chinese Academy of Sciences. His work focus on the development of the novel SERS-active substrate and biosensor for the detection of cancers.

Yusi Peng is a Ph.D. candidate at Shanghai Institute of Ceramics, Chinese Academy of Sciences. Her work focus on the development of the novel SERS substrate based on semiconductor and the biosensor based on SERS.

Jun He currently works at Anhui Provincial Center for Disease Control and Prevention. His work focus on diagnosis of virus.

Yong Yang is currently a professor at Shanghai Institute of Ceramics, Chinese Academy of Sciences. His research interests include SERS biosensor for detecting cancers and virus.